Journal of Power Sources 413 (2019) 284–292

Contents lists available at ScienceDirect

Journal of Power Sources

journal homepage: www.elsevier.com/locate/jpowsour

A detailed computational model for cylindrical lithium-ion batteries under mechanical loading: From cell deformation to short-circuit onset

Lubing Wang[a,b], Sha Yin[a,b], Jun Xu[a,b,*]

[a] Department of Automotive Engineering, School of Transportation Science and Engineering, Beihang University, Beijing, 100191, China
[b] Advanced Vehicle Research Center (AVRC), Beihang University, Beijing, 100191, China

HIGHLIGHTS

- A model describing the deformation and short-circuit onset is established.
- Constitutive models of each component are developed based on the experiments.
- Short-circuit criteria are established based on the separator failure.
- Short-circuit triggering behavior under dynamic loading is discussed.

GRAPHICAL ABSTRACT

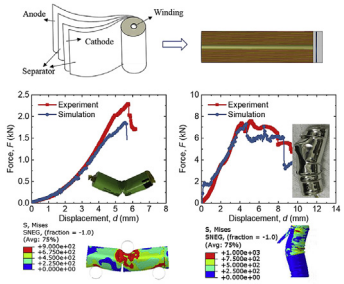

ARTICLE INFO

Keywords:
Computational model
Short-circuit criteria
Mechanical abusive loading
Lithium-ion battery

ABSTRACT

The safety design of systems using lithium-ion batteries (LIBs) as power sources, such as electric vehicles, cell phones, and laptops, is difficult due to the strong multiphysical coupling effects among mechanics, electrochemistry and thermal. An efficient and accurate computational model is needed to understand the safety mechanism of LIBs and thus facilitate fast safety design. In this work, a detailed mechanical model describing the mechanical deformation and predicting the short-circuit onset of commercially available 18650 cylindrical battery with a nickel cobalt aluminum oxide (NCA) system is established for the first time. The mechanical properties of anode, cathode, and separator are characterized. Based on the experiment results, the constitutive models of component materials are established and validated through numerical simulations. A detailed computational model including all components (i.e., separator, anode, cathode, winding, and battery casing) is then developed by evaluating four typical mechanical-loading conditions. Short-circuit criteria are subsequently established based on the separator failure, thereby enabling the mechanical model to predict the short circuit electrochemically. Results show that the model can describe LIB behaviors from mechanical deformation to internal short circuit. Results provide a powerful tool for the safety design of LIBs and related engineering systems.

1. Introduction

Lithium-ion batteries (LIBs) are widely used in portable electronic equipment, electrical vehicles, and even aircrafts owing to the environmentally sustainable needs and fast breakthroughs in energy-storage technology. However, the inevitable influence of accidents on battery-powered products may cause mechanical failure of LIB components, leading to internal short circuit, and further inducing catastrophic fire and explosion [1–3]. Such consequences pose great threats to the public and hinder the further application of LIB in the related

* Corresponding author. Department of Automotive Engineering, School of Transportation Science and Engineering, Beihang University, Beijing, 100191, China.
E-mail address: junxu@buaa.edu.cn (J. Xu).

https://doi.org/10.1016/j.jpowsour.2018.12.059
Received 6 October 2018; Received in revised form 26 November 2018; Accepted 19 December 2018
Available online 24 December 2018
0378-7753/

Nomenclature

U3	displacement in Z-direction
UR1	rotation in X-direction
UR2	rotation in Y-direction
η	stress triaxiality index
F_p	peak force
d_p	corresponding displacement of peak force
d_s	short-circuit displacement
$\sigma^{eq}_{Unified}$	equivalent stress
σ_1	first principal stress
σ_2	secondary principal stress
σ_3	third principal stress
ε_p	equivalent plastic strain
$\bar{\varepsilon}^{pl}\|_0$	initial equivalent plastic strain
ε_s	short-circuit equivalent plastic strain

field. Therefore, mechanical behaviors of LIB cell and its components are essential to battery safety and have received increasing attentions in recent years [4,5]. Most of the pioneering work and breakthroughs focused on mechanical experiments [6–8] and theoretical analysis [9] to unravel the mechanical behaviors of LIB component materials and cell structures. Some studies focus on improving the mechanical and electrical performance of the components material through new material synthesis methods [10] as well as new materials [11,12]. Previous efforts laid a strong foundation for further computational model development.

Owing to the physical complexity of LIB cells, a homogenized model that treats the inner components as a homogenized material has been developed and gradually perfected, e.g., from low [13,14] to high state-of-charge (SOC) [15], from low to high state-of-health (SOH) [16] and from quasi-static [17] to dynamic loading [15,18]. However, the homogenized model has limitations in predicting the local deformation

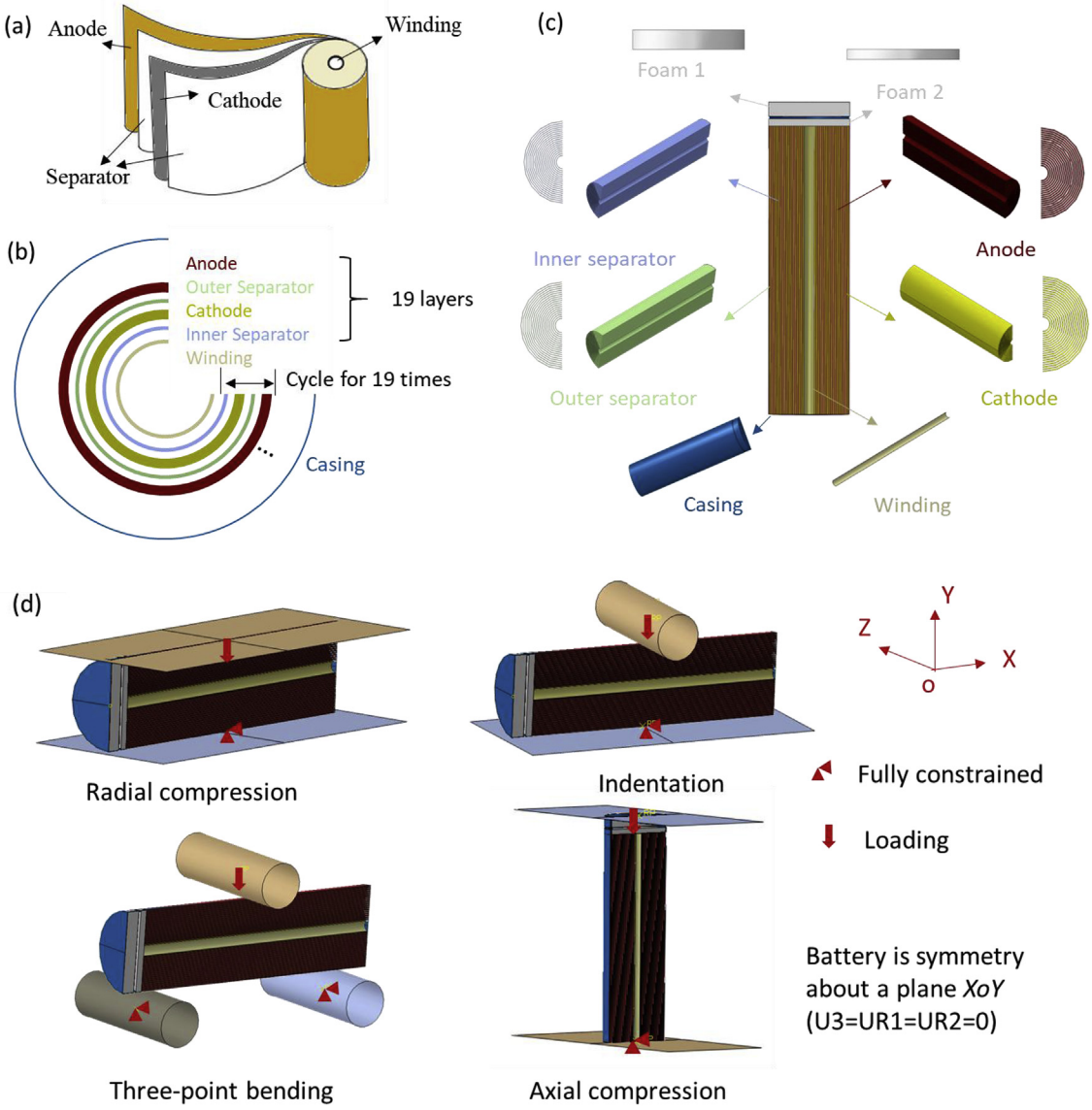

Fig. 1. Schematic geometry of the target cylindrical lithium-ion battery. (a) Macroscopic structure of the jellyroll without battery casing, (b) the concentric-circle structure of battery cell from top view, and (c) exploded view of components and their assembly. (d) Boundary-condition setups under different loading conditions for computational models (where U3, UR1 and UR2 stand for the displacement in Z-direction, rotation in X-direction, and rotation in Y-direction, respectively).

and buckling phenomenon of each components. Thus, a detailed model must investigate the deformation sequence of the cell structure and the cause of internal short circuit. Sahraei et al. [14] initiated establishing a detailed model by modeling in layers which can capture the deformation mode under radial compression. Gilaki et al. [19] developed a heterogeneous model with coincident nodes of adjacent layers merged, whose deformed shapes are consistent with the CT scans of the experiments under drop tests. Zhu et al. [20] established a detailed finite-element (FE) model, covering the geometry and the mechanical property of all components, which revealed the sequence of the axial compression. However, it can only capture the trend of the force–displacement curve but cannot predict the slope and critical inflection points of the curves under axial compression. Moreover, the concentric layered model established by Sheikh et al. [21] proved useful in predicting initial battery failures as well as deformation modes.

However, in mechanical aspect, the model can only predict the characteristic magnitude of the force, rather than the entire curve profile, thereby losing abundant critical information. The model is also incapable for predicting mechanical behavior of LIB cell in various loading scenarios. More importantly, electrochemical failure, i.e., internal short circuit is the priority of the battery safety design which has not been included in the computational mechanical model.

To better capture the local deformation of each components and understand the mechanism of mechanically induced internal short circuit, a detailed model which considers all component modeling methodologies is established in this paper. Constitutive models of each component are developed based on the designed experiments. Comprehensive validation under radial compression, bending, indentation, and axial compression are conducted and compared with corresponding experiments. Furthermore, short-circuit criteria are established based on the stress and strain distribution of the separator, and short-circuit triggering behavior under dynamic loading is discussed.

2. Computational modeling

By disassembling the battery cell, one may clearly understand the internal structure of the cylindrical battery (Fig. 1). Target 18650 cylindrical LIB is composed of battery casing, jellyroll, winding, and other gaskets, whereas the jellyroll is rolled based on a winding in a separator–cathode–separator–anode sequence (Fig. 1a). Jellyroll is simplified as concentric circles in the same sequence in 19 layers (Fig. 1b) based on the actual size in FE model. The structure after assembly is shown in Fig. 1c with the innermost layer winding and outermost layer casing, and gaskets are simplified as foams. Table 1 shows the specific geometric parameters of these components; only the size of the innermost layers of separator, anode, and cathode are presented; dimensions of remaining 18 layers can be inferred from the thickness and the innermost values.

Electrolyte is not built in the detailed model, but its effect on mechanical behaviors of anode, cathode, and separator is considered. The adopted material models of inner components are established based on the experiments when the materials are filled with electrolyte.

Battery casing, which is composed of Fe, C, and Ni, is a kind of steel whose constitutive model was established by Wang et al. recently [22]. Johnson–Cook model is adopted with strain-rate effect and Johnson–-Cook damage model. Cathode is a current collector double coated with $Li_{0.925}(Ni_{0.80}Co_{0.15}Al_{0.05})O_2$, which is modelled as an integrated part, as well as the anode. Isotropic material model is adopted for cathode and anode material; the material parameters are obtained through material tests and validated by simulation, which will be introduced in next section. Separator is a polymer material with an apparent in-plane anisotropicity [23] and different mechanical properties in tension and compression [24]. Thus, establishing the comprehensive constitutive model and time-consuming during model computation is difficult. Therefore, the isotropic elastic–plastic model is adopted for simplification. The elastic modulus of the separator, 275 MPa, refers to the tensile test in transverse direction with electrolyte effect, and the yield stress is 11.39 MPa [24]. The modulus of winding and foam are 100 GPa and 100 MPa, respectively, which are determined by simulations. Key mechanical properties are summarized in Table 2.

Shell element is used to describe battery casing and winding, whereas membrane element is used to depict the separator and the solid element describes foam, anode, and cathode. Element mesh size ranges from 0.3 to 0.8 mm for various parts, as shown in Table 3.

To simplify the helix rolling for the jellyroll, concentric circles (geometrically symmetric) are used to describe the rolling structure of jellyroll. To take advantage of symmetricity, a half FE model of battery cell is established to improve the computation efficiency. The half FE model in Fig. 1d shows the symmetry about plane *XoY*, and the bottom of the battery is fully constrained while the top end is loaded along *Y*-axis. Four typical loading conditions are established here, i.e., radial compression, indentation, three-point bending, and axial compression. To ensure a stable convergence, the general contact is adopted throughout the computation. Each run took approximately 12*h* with four CPUs for radial loadings and 144 h with 16 CPUs for axial compression.

3. Experimental

3.1. Material and specimen preparation

Commercially available 18650 NCA/graphite cylindrical LIB was chosen as target battery. All cells studied here are fresh with only one discharging cycle to zero. Nickle sheets were welded on positive and negative ends of the battery for voltage measurement. Cathode and anode were extracted from the fresh LIB cell with the electrolyte. Cathode is a current collector aluminum double coated with $Li_{0.925}(Ni_{0.80}Co_{0.15}Al_{0.05})O_2$, and anode is copper foil coating with $Li_{0.008}C_6$. The thicknesses for anode and cathode are 200 μm and 170 μm, respectively. Material samples were prepared by the metal cutter as soon as the battery was disassembled. A total of 32-layer stacks of samples with the dimension of $30 \times 30\,mm^2$ were tested.

3.2. Experimental setups

Quasi-static compression tests were carried out by Instron 8801 (Fig. 2a) with a load sensor of 100 kN and accuracy of 2 N or 0.5% force value presented. Samples were placed on a plate with a thickness of 6.86 and 5.3 mm for anode and cathode, respectively (Fig. 2b). A preload of 100 N was applied on the samples to eliminate the gap between layers. The loading speed was set as 1 mm/min. Repeated tests were conducted to ensure data credibility as shown in Fig. 2c and d.

The force of the anode increased linearly initially, entered another linear stage with a relatively lower slope, and finally failed. We infer that the collapse of the active material causes the first slope change of the curve, and the current collector Cu foil failure induces the drop of the force. Thus, a bilinear isotropic model can be used to describe this material, and the yield stress is used to capture the point when the slope changes. The force of the cathode increases almost linearly with the

Table 1
Geometric measurements of components.

	Neutral zone radius (mm)	Thickness (mm)	Length (mm)
Winding	1.14	0.16	60
Inner separator	1.228 (innermost layer)	0.016	60
Cathode	1.321 (innermost layer)	0.17	60
Outer separator	1.414 (innermost layer)	0.016	60
Anode	1.522 (innermost layer)	0.2	60
Casing	8.91	0.012	65

Table 2
Key mechanical properties of components.

Components	Material composition	Density (kg/m^3)	Modulus (MPa)	Yield stress (MPa)	Failure strain
Casing	Steel	7.85 × 103	211 000	740	η related [25]
Separator	PP/PE	1.2 × 10^3	275	11.39	1
Anode	Cu/Active material	2.27 × 10^3	300	/	/
Cathode	Al/Active material	4.68 × 10^3	720	/	/
Winding	Steel	7.85 × 10^3	100 000	2430	/
Foam	/	6.5 × 10^3	100	/	/

Table 3
Section properties and mesh information.

	Element type	Mesh size (mm)	Element number
Casing	Shell	0.8	3311
Inner separator	Membrane	0.3–0.8	32,250
Outer separator	Membrane	0.3–0.8	33,900
Anode	Solid	0.3–0.8	34,650
Cathode	Solid	0.3–0.8	32,850
Foam	Solid	0.8	1620
Winding	Shell	0.8	2160
		Total	142,000

displacement, such that the linearly elastic model is adopted to describe its mechanical behavior.

To validate the material model, FE models were established according to the material experiments. In the model, a total of 32-layer solid elements were established, and the face-to-face contact was adopted. Simulation results of anode and cathode were shown in Fig. 3a and b, respectively. The material models can well capture the elastic plastic behaviors of anode and cathode before failure. In the meantime, the deformation profile can be well depicted by computation.

3.3. Battery cell experiment

Four typical loading conditions, i.e., radial compression (Fig. 4a), indentation (Fig. 4b), three-point bending (Fig. 4c), and axial compression (Fig. 4d) were conducted to experimentally study the mechanical behavior and further discover the correlation between mechanical buckle/failure and short-circuit behaviors of the cylindrical LIB. Quasi-static loading (5 mm/min) was applied to the battery cell through the Instron 8801, and voltage was simultaneously measured by the voltage sensor (Fig. 4a). A 10 mm diameter indenter was adopted for indention and three-point bending tests, and the span of the two supports of bending test was set 50 mm as illustrated in Fig. 4b and c Three repeated tests were conducted to ensure the data credibility.

During radial compression, the force F increases linearly, and the process can be referred to as Stage I. The load then enters a platform stage referred to as Stage II, is followed by the compaction stage as Stage III, and finally drops as Stage IV (Fig. 5a). The peak force F_p is approximately 35 kN, and the corresponding displacement d_p is 6 mm. The voltage initially remains at 3.2 V and then drops to 0 V under mechanical failure. The short-circuit displacement d_s is also approximately 6 mm. Here, the phenomenon in which voltage drops to 0 V is defined as major internal short circuit, similar to Refs. [26,27].

For indentation cases, force increases gradually with the displacement as Stage I and then drops rapidly as Stage II, where F_p = 11 kN

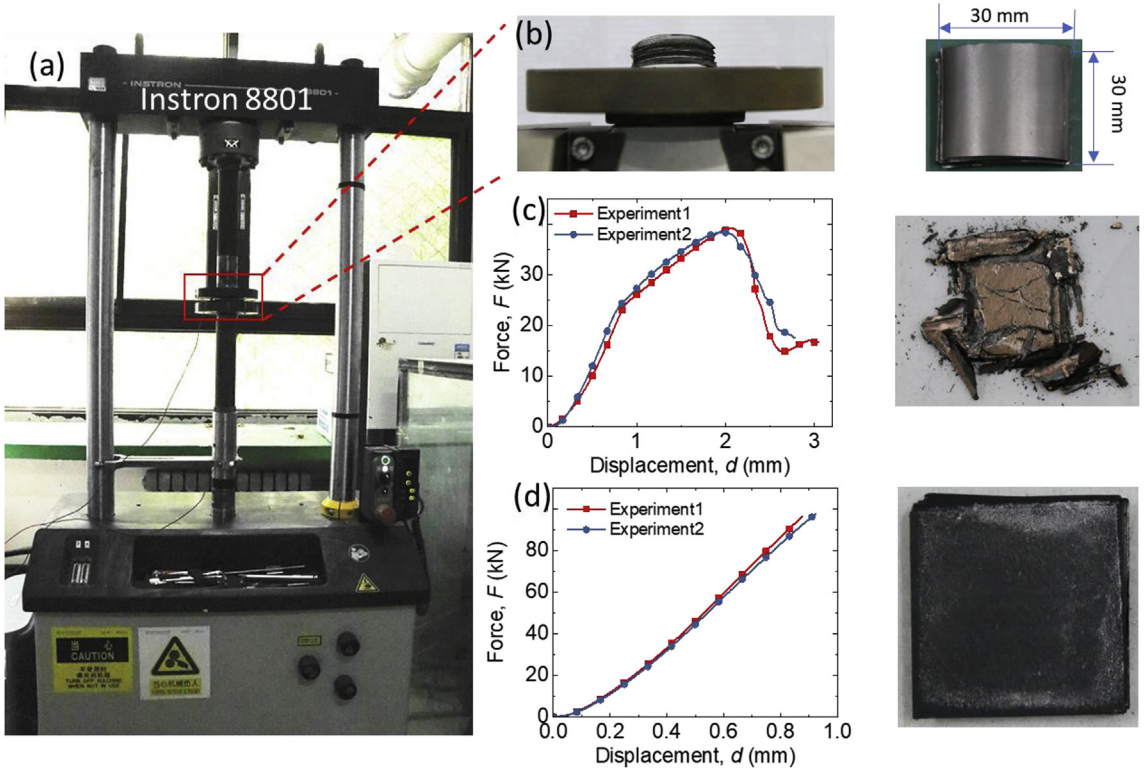

Fig. 2. Mechanical test setups for component materials of the battery. (a) Instron 8801 for mechanical loading, (b) material sample and dimension, (c) force–displacement response of anode and the sample after unloading, and (d) force–displacement response of cathode and sample after unloading.

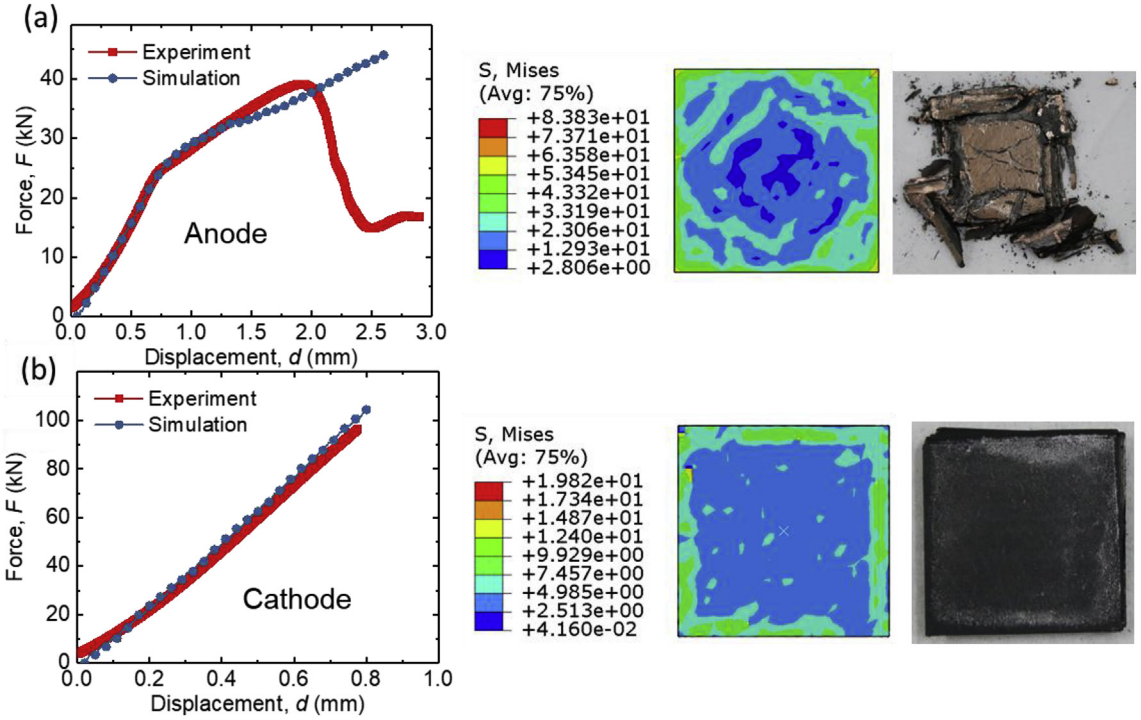

Fig. 3. Comparison of simulation results and experiments for electrodes: (a) mechanical response and deformation morphology of the anode, and (b) mechanical response and deformation profile of the cathode.

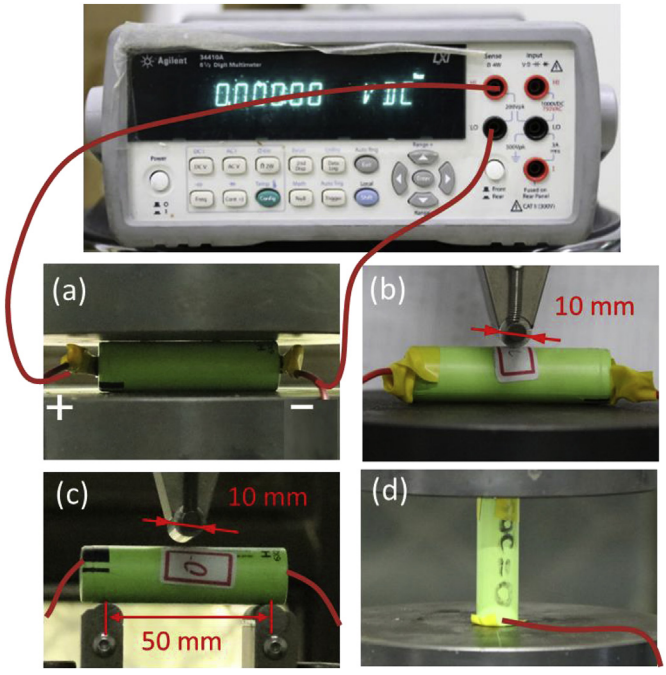

Fig. 4. Test setups for battery cell of different mechanical loading conditions with *in-situ* voltage measurement: (a) radial compression, (b) indentation, (c) three-point bending, and (d) axial compression.

and $d_p = 7$ mm (Fig. 5b). Again, the voltage remains as 3.2 V in Stage I, drops when the force drops, i.e., $d_s = 7$ mm, and recovers to 1.4 V.

For three-point bending, force increases gradually in Stage I and decreases in Stage II, where $F_p = 2$ kN and $d_p = 5$ mm. Voltage stays at approximately 3.2 V with the minor internal short circuit (voltage drops to a value larger than 0 V) occurring slightly before the peak force. The voltage remains stable despite the V-shaped structural fracture as shown in subplot of Fig. 5c. We infer that the fracture of the components cut off the minor internal short circuit to prevent further voltage drop.

For axial compression, Fig. 5d shows that the force increases almost linearly in Stage I until reaching the peak force. The force then fluctuates around 7 N because the casing buckles layer-by-layer in Stage II and finally drops for the complete fracture of the casing in Stage IV. Buckle rings form mainly in Stage II, and a large crack forms in Stage III, evidenced by the photo of the battery cell after loading in Fig. 5d.

To summarize, mechanical buckling behavior has a strong influence over the short-circuit behavior; therefore, having an accurate prediction for mechanical behavior and a good understanding of short-circuit onset is important.

4. Results and discussion

4.1. Simulation results and validation

To validate the above-mentioned computational model, simulation results are compared with the experiment data shown in Fig. 6. For radial compression, force in simulation can capture the general trend of the experiment except for Stage II, where the force prediction is larger than the experiment (Fig. 6a). The deformation profile and the stress distribution are obtained from the simulation, which shows a good agreement with the experiment. The stress on the edges of the battery is larger than anywhere else because these areas are in contact with the pressure plate. For indentation, simulation can well predict the mechanical response before failure (Fig. 6b). The deformation mode is similar with the experiment, especially the bending and buckle profile, and the maximum stress occurs at the center of battery owing to the indenter. For three-point bending, the force in simulation can well predict the force evolution with displacement including the force turning point and the failure point (Fig. 6c). However, the predicted force is smaller than the experimental value when the displacement is larger than 5 mm because the general contact algorithm allows some minor penetration. The deformation profile of the cell highly agrees with experiment as well as the failure crack. The stress distribution

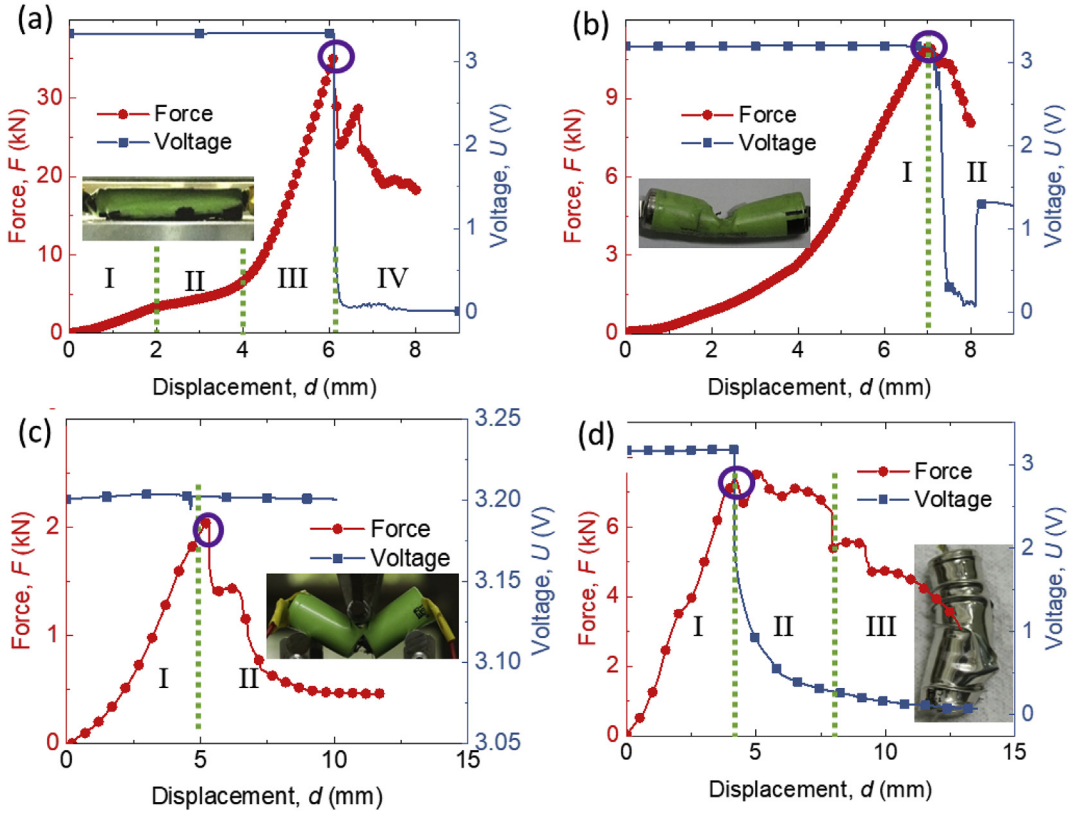

Fig. 5. Force–displacement, voltage–displacement curves, and corresponding failure profiles of battery cell experiments under (a) radial compression, (b) indentation, (c) three-point bending, and (d) axial compression loading conditions.

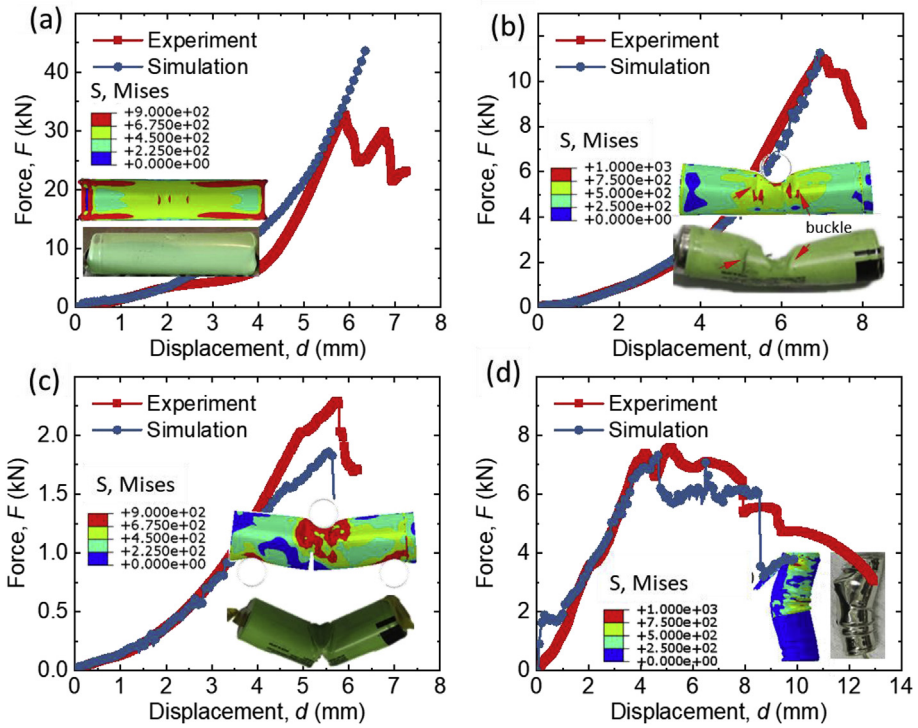

Fig. 6. Comparison between simulation and experiments in terms of mechanical response and deformation modes under (a) radial compression, (b) indentation, (c) three-point bending, and (d) axial compression loading conditions.

shows that the areas in contact with the indenter suffer from the larger stress. For axial compression, Fig. 6d shows the force response can be well captured by the computation, including the peak force, force fluctuation, and failure evolution. The numerical simulation results can also predict the buckle rings and the failure modes.

This detailed model of the cylindrical battery can well capture the mechanical response during different loading conditions, thereby proving its accuracy and versatility. However, some shortcomings cannot be avoided. For radial compression and indentation, this model cannot capture the mechanical failure characteristics of the cell because the failure model of battery casing is established based on the tensile tests. However, the crack of the battery occurs on the two ends of the battery casing which is caused by compressive stress for radial compression, whereas the failure of the battery casing in indentation is caused by the shear stress. Establishing a mechanical failure criterion for the jellyroll itself remains difficult.

4.2. Short-circuit criteria

Internal short circuits are caused by the direct contact between anode and cathode with either the active material or current collector, and they are defined as four internal short-circuit modes [28,29]. The separator, placed between the anode and cathode to avoid their direct contact, is a critical factor in causing the internal short circuit. Therefore, two short-circuit criteria are established based on the mechanical properties of the separator through the detailed model in the scenario of mechanical loading induced internal short circuit, i.e., stress state-based and strain state-based criteria. For stress state-based criterion, the unified strength theory (UST) which is a generalized form of von Mises, Tresca, and Mohr–Coulomb criteria with consideration of three principal stresses is adopted [30] as follows:

$$\sigma^{eq}_{Unified} = 16.125\ \text{MPa} = \begin{cases} \sigma_1 - 0.0135(\sigma_2 + \sigma_3), & \sigma_2 \le \frac{\sigma_1 + 0.027\sigma_3}{1.027} \\ 0.5(\sigma_1 + \sigma_2) - 0.027\sigma_3, & \sigma_2 \ge \frac{\sigma_1 + 0.027\sigma_3}{1.027} \end{cases} \quad (1)$$

The values of $\sigma^{eq}_{Unified}$ can be determined by extracting three principle stresses of separator for different loading conditions shown in Fig. 7a. The results show that this criterion is suitable for these four loading conditions.

For strain state-based criterion, equivalent plastic strain ε of all separator nodes are extracted from four loading conditions and plotted in Fig. 7b. Each node which is numbered sequentially has its own equivalent plastic strain. Equivalent plastic strain ε can be calculated as:

$$\varepsilon = \bar{\varepsilon}^{pl}|_0 + \int_0^t \sqrt{\frac{2}{3}\dot{\varepsilon}^{pl}:\dot{\varepsilon}^{pl}}\,dt \quad (2)$$

where $\bar{\varepsilon}^{pl}|_0$ is the initial equivalent plastic strain. $\varepsilon_s = 0.95$ is the strain state-based criterion which can well predict the short-circuit behavior of indentation, radial compression, and axial compression. However, it cannot predict the minor short-circuit behavior of the bending test owing to different trigger mechanisms.

We conclude that stress state-based criterion is suitable for predicting minor and major internal short circuits, whereas the strain state-based criterion is only suitable for major internal short circuits. However, the strain state-based criterion is much more convenient for the reader to use without any extra calculations.

4.3. Short-circuit triggering under dynamic loading

To investigate the mechanical and electrical behaviors of the battery under dynamic loading, drop tests with the hammer of 49.74 kg are conducted. Force and voltage are synchronous recorded by an oscilloscope with 1.25 MHz. Experimental results are shown in Fig. 8 with force–time and voltage–time curves under different impact velocities. Voltage decreases then recovers at the impact speed of 1 m/s (Fig. 8a), whereas the voltage drops close to 0 V when the impact speed larger than 1.2 m/s (Fig. 8b and c). We infer that the critical failure energy of the LIB is 25–36 J which is much smaller than 46 J under quasi-static loading. Force evolution under dynamic loading is similar with quasi-static loading with four stages noted in Fig. 8a. Moreover, the major internal short circuit occurs, and the force drops simultaneously. To compare the short-circuit triggering with dynamic and quasi-static loadings, force–time curves under dynamic loading are translated into force–displacement curves according to Newton's second law, as shown in Fig. 8d. The internal short circuit under dynamic loading occurs earlier than its counterpart under quasi-static loading. Simulations under dynamic loading are conducted to explain this phenomenon. The first step is to validate the mechanical model and the short-circuit criteria under dynamic loading, and the results are shown in Fig. 8e. The detailed model can capture the trend of the force–time response and peak force. Moreover, the strain state based short-circuit criteria can also predict the short-circuit triggering time. The short-circuit displacement under dynamic loading is then discussed based on the simulation (Fig. 8f). Results show that short-circuit displacement under dynamic loading is approximately 5 mm; it is not influenced by the impact velocity but is smaller than the quasi-static loading. This phenomenon can be explained by the strain-rate effect of battery casing which has high strength suffering from dynamic loading. The high stress is transmitted to the inner components, causing the large strain and eventually leading to earlier internal short circuit. However, the range of the strain rate is small in dynamic loading, such that its effect on short-circuit triggering is negligible.

5. Conclusion

A detailed model of the 18650 cylindrical battery cell that can well predict the mechanical behaviors of the cell under radial compression, indentation, bending, and axial compression is established in this paper.

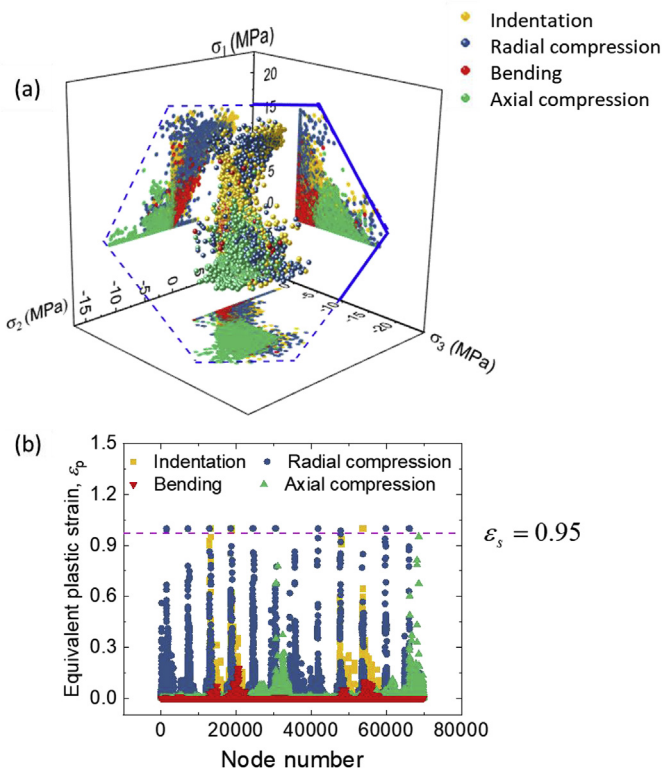

Fig. 7. Calibration of the two proposed short-circuit criteria in various loading conditions: (a) short-circuit criterion based on the UST and final criteria yield plane illustration, and (b) strain state-based short-circuit criterion along with the final criterion yield line indication ($\varepsilon_s = 0.95$).

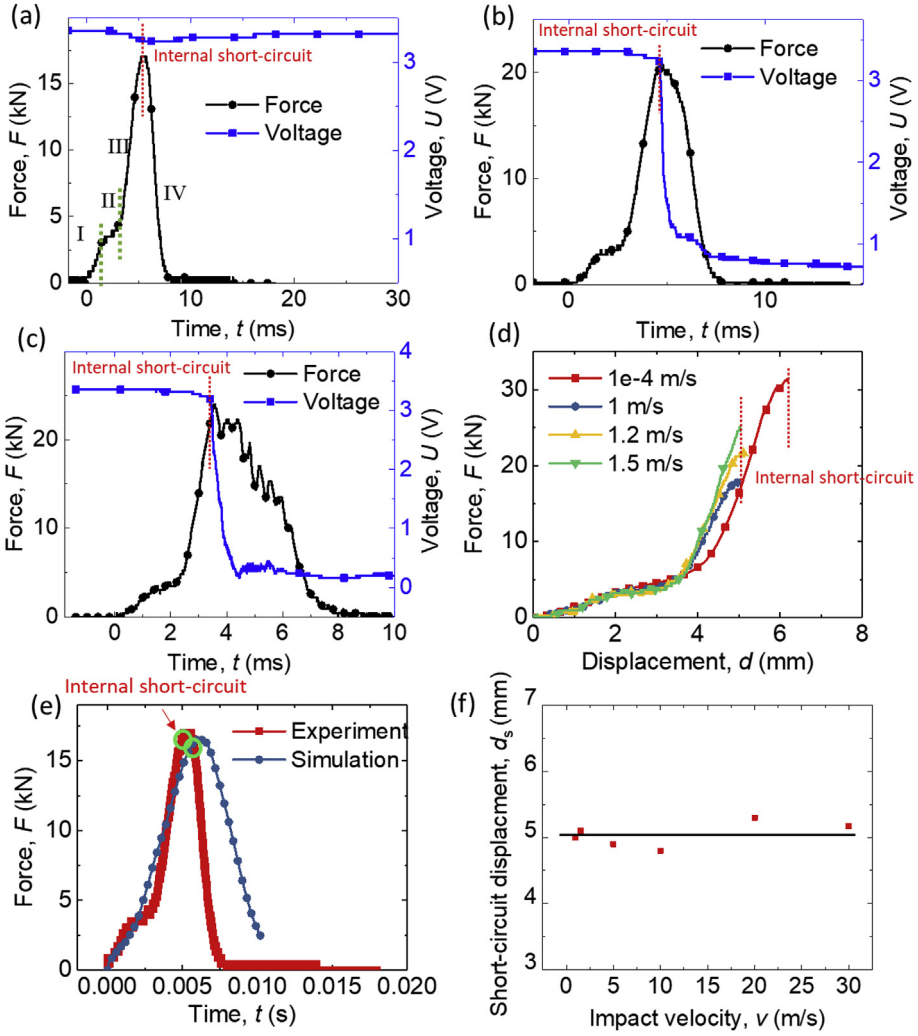

Fig. 8. Experimental results of battery cell under dynamic loading with a hammer mass of 49.74 kg. Force–time and voltage–time curves of different impact speeds at (a) 1 m/s, (b) 1.2 m/s, and (c) 1.5 m/s. (d) Comparison of force–displacement curves and internal short-circuit displacement under quasi-static and dynamic loadings. Simulation results under dynamic loading: (e) comparison of experiment and simulation at an impact speed of 1 m/s. (f) Short-circuit displacement–impact velocity curve based on strain-state criteria.

The deformation modes of cells under these loading conditions can be well captured. The failure properties can also be predicted when the failure of the battery cell is caused by the tensile stress such as in the scenarios of three-point bending and axial compression. Moreover, two short-circuit criteria are established and compared based on the computational model. Stress state-based criterion is useful for predicting the short-circuit behavior whether minor or major internal short circuit, whereas the strain state-based criterion is convenient for use but has limitations in predicting the minor internal short circuit. Finally, short-circuit triggering point under dynamic loading is studied by experiments and simulations.

The established computational model, together with suggested internal short-circuit criteria pave a new pathway for battery cell, module and pack safety design upon mechanical abusive loading.

Conflicts of interest

There are no conflicts to declare.

Author contribution

J.X. conceived the study. L.W. conducted the experiment and established FE model. S. Y., L.W. and J.X. analyzed the data and wrote the manuscript.

Acknowledgement

This work is financially supported by The National Science Foundation of China (11872099), National Key Research and Development Program of China (2017YFB0103703), Opening project of State Key Laboratory of Explosion Science and Technology (Beijing Institute of Technology) with project number of KFJJ17-13M.

References

[1] X. Feng, M. Fang, X. He, M. Ouyang, L. Lu, H. Wang, M. Zhang, J. Power Sources 255 (2014) 294–301.
[2] F. Ren, T. Cox, H. Wang, J. Power Sources 249 (2014) 156–162.
[3] T.Y. Lu, C.C. Chiang, S.H. Wu, K.C. Chen, S.J. Lin, C.Y. Wen, C.M. Shu, J. Therm. Anal. Calorim. 114 (2013) 1083–1088.
[4] J. Zhu, T. Wierzbicki, W. Li, J. Power Sources 378 (2018) 153–168.
[5] T.H. Dubaniewicz, J.P. DuCarme, IEEE Trans. Ind. Appl. 49 (2013) 2451–2460.
[6] X. Zhang, T. Wierzbicki, J. Power Sources 280 (2015) 47–56.
[7] E. Sahraei, R. Hill, T. Wierzbicki, J. Power Sources 201 (2012) 307–321.
[8] I. Avdeev, M. Gilaki, J. Power Sources 271 (2014) 382–391.
[9] T. Wierzbicki, E. Sahraei, J. Power Sources 241 (2013) 467–476.
[10] L. Ouyang, Z. Cao, H. Wang, R. Hu, M. Zhu, J. Alloy. Comp. 691 (2017) 422–435.
[11] C. Lin, R. Hu, J. Liu, L. Yang, J. Liu, L. Ouyang, M. Zhu, J. Alloy. Comp. 763 (2018) 296–304.

[12] M. Zhang, R. Hu, J. Liu, L. Ouyang, l. Jun, L. Yang, F. Fang, M. Zhu, J. Alloy. Comp. 762 (2018) 246–253.
[13] L. Greve, C. Fehrenbach, J. Power Sources 214 (2012) 377–385.
[14] E. Sahraei, J. Campbell, T. Wierzbicki, J. Power Sources 220 (2012) 360–372.
[15] J. Xu, B. Liu, X. Wang, D. Hu, Appl. Energy 172 (2016) 180–189.
[16] J. Xu, Y. Jia, B. Liu, H. Zhao, H. Yu, J. Li, S. Yin, Exp. Mech. 58 (2018) 633–643.
[17] W. Wang, S. Yang, C. Lin, Appl. Energy 196 (2017) 249–258.
[18] Y. Jia, S. Yin, B. Liu, H. Zhao, H. Yu, J. Li, J. Xu, Energy 166 (2019) 951–960.
[19] M. Gilaki, I. Avdeev, J. Power Sources 328 (2016) 443–451.
[20] J. Zhu, X. Zhang, E. Sahraei, T. Wierzbicki, J. Power Sources 336 (2016) 332–340.
[21] M. Sheikh, A. Elmarakbi, M. Elkady, J. Power Sources 370 (2017) 61–70.
[22] L. Wang, S. Yin, Z. Yu, Y. Wang, T.X. Yu, J. Zhao, Z. Xie, Y. Li, J. Xu, Mater. Des. 160 (2018) 601–610.
[23] J. Xu, L. Wang, J. Guan, S. Yin, Mater. Des. 95 (2016) 319–328.
[24] J. Cannarella, X.Y. Liu, C.Z. Leng, P.D. Sinko, G.Y. Gor, C.B. Arnold, J. Electrochem. Soc. 161 (2014) F3117–F3122.
[25] L. Wang, S. Yin, Z. Yu, Y. Wang, T.X. Yu, J. Zhao, Z. Xie, Y. Li, J. Xu, Mater. Des. 160 (2018) 601–610.
[26] X.W. Zhang, E. Sahraei, K. Wang, Sci. Rep.-UK 6 (2016) 9.
[27] C. Zhang, S. Santhanagopalan, M.A. Sprague, A.A. Pesaran, J. Power Sources 290 (2015) 102–113.
[28] W. Zhao, G. Luo, C.Y. Wang, J. Electrochem. Soc. 162 (2015) A1352–A1364.
[29] S. Santhanagopalan, P. Ramadass, J. Zhang, J. Power Sources 194 (2009) 550–557.
[30] J. Xu, B. Liu, L. Wang, S. Shang, Eng. Fail. Anal. 53 (2015) 97–110.